Design, Simulation, Fabrication, and Preliminary Tests of 3D CMS Pixel Detectors for the Super-LHC

Ozhan Koybasi, Daniela Bortoletto, Thor-Erik Hansen, Angela Kok, Trond Andreas Hansen, Nicolas Lietaer, Geir Uri Jensen, Anand Summanwar, Gino Bolla, and Simon Wing Lok Kwan

Abstract— **The Super-LHC upgrade puts strong demands on the radiation hardness of the innermost tracking detectors of the CMS, which cannot be fulfilled with any conventional planar detector design. The so-called 3D detector architectures, which feature columnar electrodes passing through the substrate thickness, are under investigation as a potential solution for the closest operation points to the beams, where the radiation fluence is estimated to reach 10^{16} n_{eq}/cm^2. Two different 3D detector designs with CMS pixel readout electronics are being developed and evaluated for their advantages and drawbacks. The fabrication of full-3D active edge CMS pixel devices with p-type substrate has been successfully completed at SINTEF. In this paper, we study the expected post-irradiation behaviors of these devices with simulations and, after a brief description of their fabrication, we report the first leakage current measurement results as performed on wafer.**

Index Terms— **3D silicon pixel detectors, CMS, radiation hardness, Super-LHC.**

I. INTRODUCTION

CERN is planning to upgrade the LHC to run at a peak luminosity of 10^{35} cm^{-2}s^{-1} which is one order of magnitude higher than that of the current operation in order to improve the chances of discovering new high energy particles and enable more precise measurements. The high luminosity upgrade of LHC -referred to as Super LHC or SLHC- entails the tracking devices operated at radii of ~ 4 cm to withstand a radiation fluence of 10^{16} n_{eq}/cm^2. The silicon detectors currently installed at innermost layers of the LHC trackers are designed to cope with radiation fluences of up to 10^{15} n_{eq}/cm^2. The limitations of the present detector technology have initiated the search for novel detector concepts, architectures, and materials to meet radiation hardness requirements of the Super-LHC, exhibiting the same tracking and vertexing performance as the LHC detectors to achieve the physics goals. 3D detector geometries proposed by S. Parker (1995) [1] are promising developments for the innermost tracker layers of the next generation experiments.

II. 3D DETECTOR ARCHITECTURES

The radiation hardness of a semiconductor detector is mainly determined by its electrode spacing as well as the sensor material properties. In a conventional planar detector, the two sets of electrodes are implanted on the opposite surfaces of the chip with readout electrodes segmented in the form of strips or pixels. This geometry makes the n-type and p-type electrode separation, and therefore, the carrier drift distance equal to the substrate thickness. Thus, the drift distance cannot be decreased without reducing the substrate thickness. However, a reasonable substrate thickness must be maintained to allow enough charge generation by the ionizing radiation, which is required for a good signal-to-noise ratio. Therefore, there is a tradeoff between radiation hardness and signal-to-noise performance for planar detectors. In a 3D detector, on the other hand, the n-type and p-type electrodes are arrays of columns that penetrate into the bulk. This architecture allows an electrode spacing of as small as ~ 30 μm in a substrate with a thickness comparable to that of a typical planar detector (200-300 μm), leading to superior radiation hardness without sacrificing the signal-to-noise ratio significantly. The geometries and operations of a planar detector and a 3D detector are compared in Fig.1.

The fabrication of 3D detectors is much more complicated than that of planar detectors. It requires a reactive ion etching of the electrodes into the bulk and bonded support wafer to maintain the wafer integrity after hole etching. Due to the challenges arise in the fabrication of full 3D detectors, alternative structures, including single-type column (STC) 3D detectors [2-9] and double-sided 3D detectors [10-15], have been proposed and studied to simplify the manufacturing process although they were not expected to be as radiation-

O. Koybasi is with the Department of Physics and Birck Nanotechnology Center, Purdue University, West Lafayette, IN 47907 USA (phone: 765-494-4899; e-mail: okoybasi@purdue.edu).

D. Bortoletto and G. Bolla are with the Department of Physics, Purdue University, West Lafayette, IN 47907 USA (e-mail: bortolet@purdue.edu).

T. E. Hansen, A. Kok, T.A. Hansen, N. Lietaer, G. U. Jensen, and A. Summanwar are with SINTEF, SINTEF MiNaLab, Blindern, 0314 Oslo, Norway (e-mail: Thor-Erik.Hansen@sintef.no)

S. W. L. Kwan is with Fermilab, Batavia, IL 60510-5011 USA (e-mail: swalk@fnal.gov)
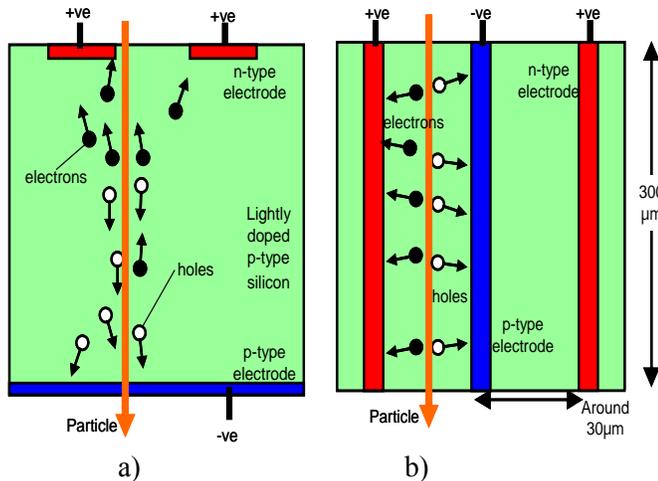
hard as full 3D detectors.

Fig.1.a) Planar detector: Vertical carrier drift with a drift distance equal to substrate thickness. Vertical depletion with depletion voltage α (substrate thickness)² b) 3D detector: Sideway charge collection with a drift distance equal to column spacing and independent of substrate thickness. Lateral depletion with a depletion voltage α (column spacing)².

In STC-3D detectors, electrodes of one type are fabricated as columns whereas electrodes of the other type are ion implanted on the back surface. Therefore, the process of etching holes and filling trenches with polysilicon has to be carried out only once. Moreover, the columns do not pass through the full substrate thickness, simplifying the fabrication further as it eliminates the need for the initial bonding and final removal of a support wafer. In STC-3D devices, the radiation-induced electrons drift to the nearest column and get collected while the holes have to traverse the entire substrate thickness to get collected by the back surface, resulting in a relatively slow full charge collection.

In double-sided 3D sensors, the n-type columns fabricated from the front and used for readout while p-type columns are fabricated from the back-side and used for biasing. This makes the processing of double-sided 3D detectors easier compared to the conventional full 3D detectors, in which the two sets of columns are fabricated from the same side. Moreover, in double-sided 3D devices, neither set of columns goes through the entire substrate thickness, which increases the resistance to mechanical stress and does not require a supporting wafer. The main weakness of double-sided 3D detectors is the presence of low electric field regions near the front and back surfaces. After heavy radiation, it becomes hard to deplete these regions, resulting in charge loss [11].

First full 3D detectors were fabricated at Stanford Nanofabrication Facility in 1997 [16]. Recently, the processing has been transferred to SINTEF for larger scale production as a part of the 3D Collaboration which now includes the University of Manchester, SLAC, Purdue University, University of Hawaii, Oslo University, CNM-Barcelona, FBK-Trento, and SINTEF. Stanford still contributes with polysilicon filling and consulting.

In a planar detector, the front and back surfaces are at different potentials, and the cutting edge of the sensor is conductive and a source of high leakage current due to the

non-passivated dangling bonds. In order to keep the electric field in the active area away from the cracks and dangling bonds of the dice line, some space must be left between the boundary of the sensitive region and the physical edge. Moreover, the passivating oxide has a fixed positive charge that resides near the silicon/oxide interface and induces an electron channel on the silicon surface. Further space must be allocated for guard rings to cutoff this conductive channel and thereby allow a uniform potential drop along the sensor periphery, preventing breakdown. The detector edges are dead regions and can cover hundreds of microns of the detector's surface area.

In 3D detectors, on the other hand, since the front and back surfaces are at the same potential, a conductive edge does not present an issue. Therefore, 3D sensors can be fabricated with an active edge electrode [17-19] that increases the sensor sensitivity to within a few microns of the physical edge. The active edge electrode is formed by etching the chip periphery through the wafer with a deep reactive ion etching tool and filling the trench with doped polysilicon. Stanford and SINTEF 3D sensors use active edge electrodes. In fact, the conventional planar detectors can be fabricated with an active edge instead of guard rings (planar 3D detectors) but these detectors are not suitable for high radiation environments [20].
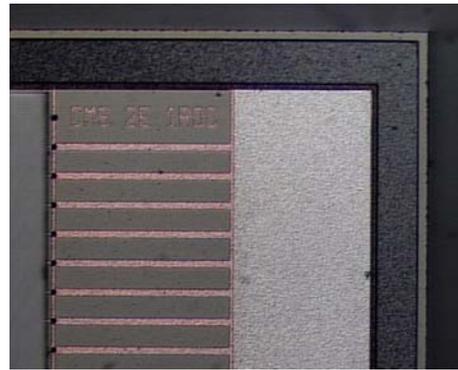

Fig.2 A picture showing the active edge of a 3D CMS sensor fabricated at SINTEF.

The functionality of p-type active edge is different for 3D detectors made on n-type and p-type substrates with n-type readout electrodes. In the case of n-type substrate, all pixels have a common p-n junction via the p-type bias electrodes. The p-n junction also includes the p-spray layers on the top and bottom surfaces and the active edge. Therefore, when the wafer is diced through the p-spray, the depletion region extends to the cutting edge, leading to an enormous increase in the leakage current. In the case of p-type substrate, on the other hand, the pixels are decoupled and the p-spray layers are not a part of a p-n junction so the active edge prevents the space-charge region from reaching out to the saw line.

3D CMS Pixel Layouts

Two different 3D sensor layouts which feature different number of columns per pixel are used for the CMS as shown in Fig.3. The 100μm by 150μm CMS pixel size contains two

readout electrodes (2E) in one layout and four readout electrodes (4E) in the other. The readout electrodes consist of n-type columns which are shorted together in each pixel. Each n-type column is surrounded by four biasing p-type columns, forming sub-pixels. All the p-electrodes are connected by a patterned metal layer to a b ias pad. A single CMS chip contains ~2000 pixels with ~4000 and ~8000 n-type electrodes in the 2E and 4E geometries, respectively.
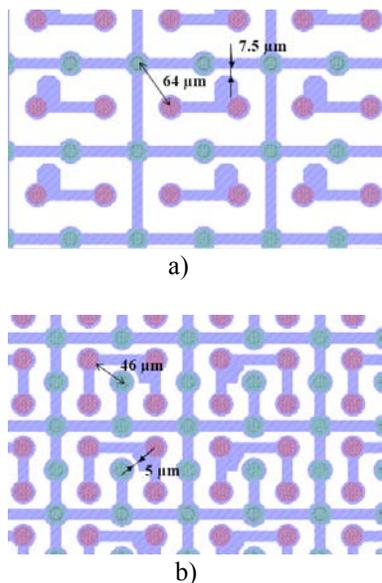

Fig.3 Layouts of 3D CMS pixel detectors with: a) 2 electrodes per pixel (2E); b) 4 electrodes per pixel (4E).

The dimensions of a single cell in the 4E configuration are 25 μm by 37.5 μm whereas the 4E configuration has a cell size of 50 μm by 37.5 μm. Different electrode spacing ascribes both advantages and disadvantages to each layout. Although the 4E geometry gives rise to a lower depletion voltage, faster response and less carrier trapping, one of its drawbacks is the higher pixel capacitance which results in a poorer signal-to-noise ratio. Furthermore, as will be discussed later in section 4, a negligible portion of the charge generated in the bias and readout columns is collected at high radiation fluences so the dead volume in the 4E configuration will be as twice as that of the 2E configuration.

III. SIMULATIONS OF 3D CMS PIXEL DETECTORS WITH RADIATION DAMAGE

A. Modeling of Radiation Damage

The incident radiation does not interact only with the electron clouds surrounding the silicon nuclei, but also with the nuclei themselves and if the radiation particle has sufficient energy to provide the required recoil energy to remove an atom from its lattice, the silicon atom will be kicked out of its lattice, placing a cr ystal defect. The resulting empty lattice sites are called vacancies and the atoms between the regular lattice sites are called interstitials. Most of the primary radiation-induced defects are not stable. Vacancies and interstitials move through the crystal at room temperature and

partially anneal if they meet and recombine during their immigration. However, some energetic displaced lattice atoms may also lead to secondary processes, forming stable defect clusters that alter the electrical properties of silicon. Besides introducing bulk defects, the ionizing radiation leads to an increase of the fixed oxide charge near the silicon/oxide interface, which saturates at ~1×10^{12} cm^{-2} after radiation doses of some kilograys.

The main manifestations of the stable crystal defects in the detector performance are increase of leakage current, change of effective space-charge density in the space charge region and a consequent increase of depletion voltage, and trapping of charge carriers. The rise of leakage current is due to electron-hole pair generation via the allowed electronic states near the center of the band gap introduced by lattice defects. The deep level defects above the mid band gap are mostly unoccupied because of the lack of free carriers in the space-charge region. The small occupied portion of these recombination-generation centers will be in a negatively charged state, increasing the effective p-type doping of silicon while the dominating unfilled states can trap free electrons from the conduction band. Similarly, most of the defect states below the mid band gap are filled with electrons and can trap holes from the valence band.

A radiation damage model for p-type float zone (FZ) silicon with three trap levels (two acceptor levels positioned slightly above the mid ban gap for increase of leakage current, change of effective doping concentration, and trapping of holes and one donor level located far below the band gap for trapping of holes) has been proposed [21]. The leakage current and depletion voltage simulations done by employing this model have shown a v ery good agreement with the experimental results for p-type planar detectors.

In order to improve the accuracy of the trapping rates, the carrier cross sections in the original model were later modified in Ref.[22]. The model was applied to an n-on-p pad detector to check how the modification of the parameters affects the accuracy of depletion voltage and leakage current. The depletion voltage is still predicted with a good accuracy. Although the simulated damage constant was about 30% higher than the experimental value, the result is satisfactory since the measured damage constant can vary by more than 30% under different annealing conditions. The simulated charge collection efficiencies using the modified model follow the same trend as the experimental results for both an n-on-p strip detector and a 3 E ATLAS 3D detector, confirming the geometry independence of functionality of the model. At fluences of ~1×10^{15} n$_{eq}$/cm^2, the experimental and simulated charge collection efficiencies match but at higher fluences, the simulated values drop to about 60-70 % of the experimental data. Similar behavior was observed with some other models such as Ref. [23].

B. Simulations of 3D CMS Pixel Detectors with Synopsys Sentaurus

Numerical simulations have been carried out with Synopsys Sentaurus TCAD [24] to predict the post-irradiation electrical

and charge collection performance of the 3D CMS detectors. The electron, hole, potential and space charge distributions are found by solving simultaneously the Poisson's equation and the continuity equations for electrons and holes. The Poisson's equation, which relates charge density and potential, takes into account all charges associated with electrons, holes, donors and acceptors, and deep level defect states. The carrier continuity equations relate drift, diffusion, and recombination and generation through the deep level defects, which is described by Shockly-Read-Hall (SRH) statistics. A trap is characterized by its type (donor-like or acceptor-like), its energy level, the related defect, and its carrier cross sections. Sentaurus can simulate the effects of radiation damage once the parameters of the traps and their concentrations, which are linearly proportional to the radiation fluence, are specified.

3D simulations are extremely slow but the pixel's symmetry makes it p ossible to obtain information about depletion voltages, breakdown behavior and charge collection efficiency, as long as the charge sharing between neighboring pixels is ignored, by performing the simulations with only a single cell. In ref.[25], it has been shown that the charge sharing is reduced in 3D structures. In all simulations of 3D CMS detectors, a s ubstrate thickness of 200 μm, a substrate doping of $7x10^{11}$ cm^{-3} (corresponding to a resistivity of ~19 kΩ.cm) and a column diameter of 14 μm are assumed. The p-spray concentration at the silicon/oxide interfaces is set in such a way that it matches the inversion charge concentration after the oxide charge reaches its saturation value which will be taken $1x10^{12}$ cm^{-2} throughout all the simulation work. The simulated cell of the 4E CMS pixel geometry is shown in Fig.4.
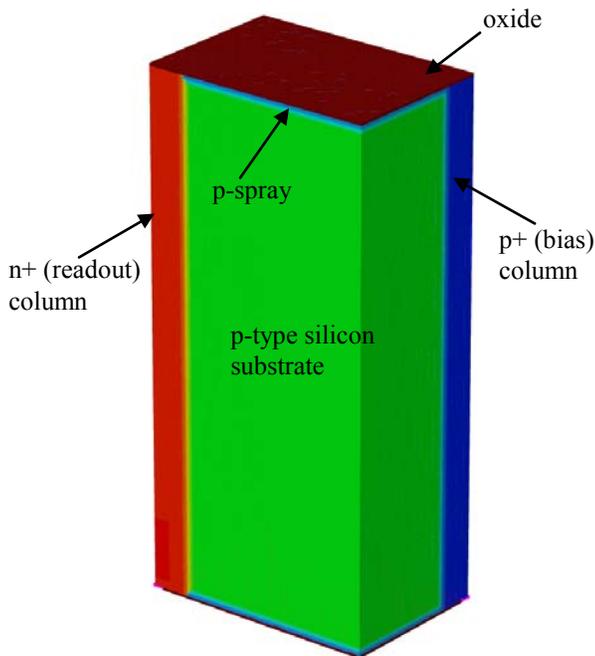

Fig.4 The one-cell input structure used in the simulation of the 4E CMS pixel sensor. The ratio of x-y scale to z (vertical)-scale is 2.5.

Fig.5 shows the simulated depletion voltage as a function of radiation fluence for each of the 3D CMS pixel geometries.

The regions near the front and back surfaces deplete more slowly as the p-side of the p-n junction is more heavily doped at the locations of the p-spray layers. At fluence of $1x10^{16}$ n_{eq}/cm^2, 2E and 4E configurations have full depletion voltages of 220 V and 80 V, respectively. For comparison, it would take 2000-3000 V to fully deplete a typical planar detector made with p-type substrate at this fluence.
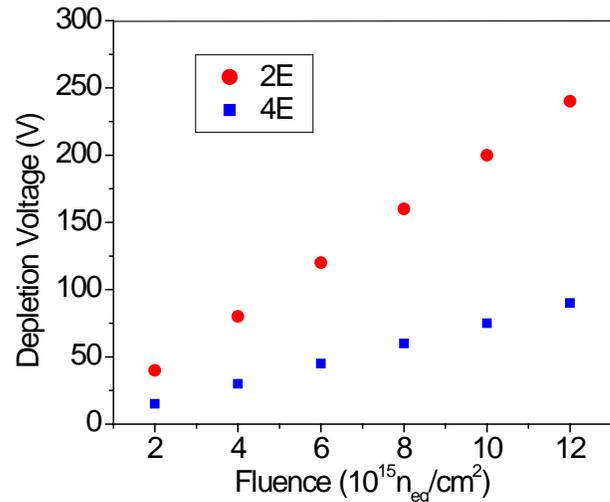

Fig.5 Depletion voltages of 3D CMS pixel detectors as a function of radiation fluence.

The maps of electric field distributions at fluence of $1x10^{16}$ n_{eq}/cm^2 (Fig..6) have shown too low electric fields at the corners of the mesh, the midway between two neighboring n-type columns or p-type columns. The electric field maxima are located around the n-electrodes where the p-n junction is located. The top and bottom portions of the p-n junction (not shown), where the p-side is the p-spray layers, have highest electric spots that determine the breakdown. Moreover, as the cell size increases, the uniformity of electric field degrades so the 4E configuration has a more even field distribution.

The pre-irradiation and post-irradiation breakdown behaviors of 2E and 4E configurations have been simulated using the impact ionization model proposed by Okuto and Crowell [26]. In Fig.7, leakage currents versus reverse bias voltage for each structure at fluences of zero and $1x10^{16}$ n_{eq}/cm^2 are shown. The oxide charge was taken $1x10^{11}$ cm^{-2} before irradiation whereas it was assumed to saturate at $1x10^{12}$ cm^{-2} after irradiation. Comparing the post-irradiation breakdown voltages of 330 V and 400 V with the depletion voltages obtained previously from the simulations, it seems theoretically possible to operate both geometries at full depletion at the high SLHC fluences without undergoing a breakdown. However, the larger difference between its breakdown voltage and depletion voltage makes the 4E configuration more reliable. To be precise, the difference between the breakdown voltage and full depletion voltage is as high as 320 V for the 4E layout whereas it is 110 V for the 2E
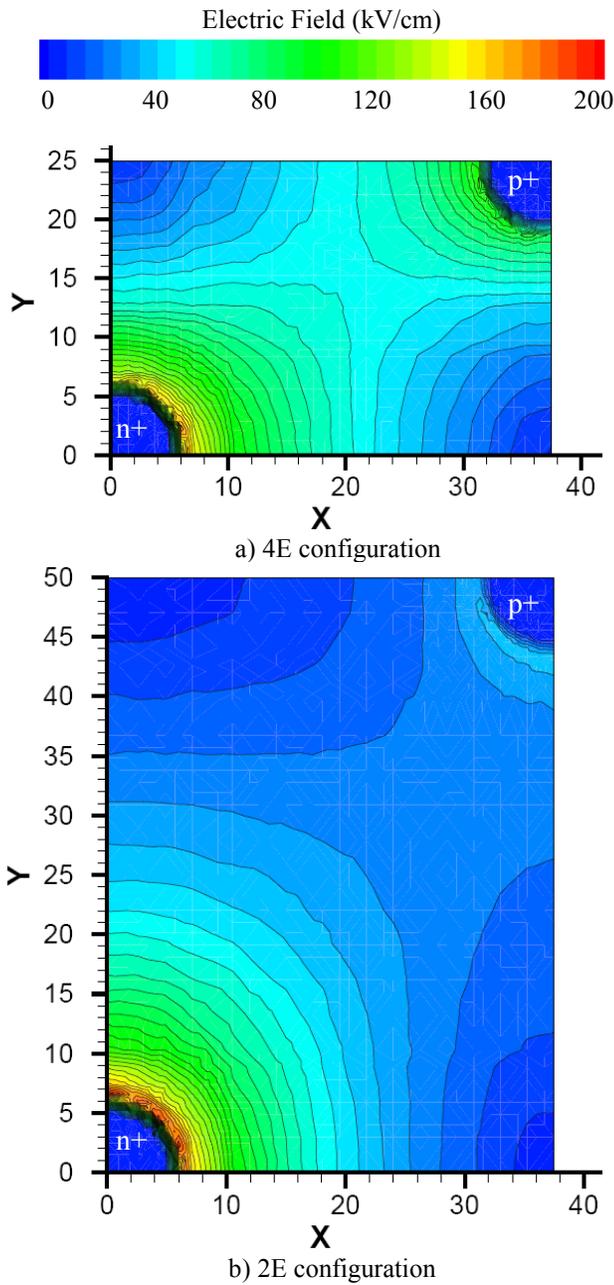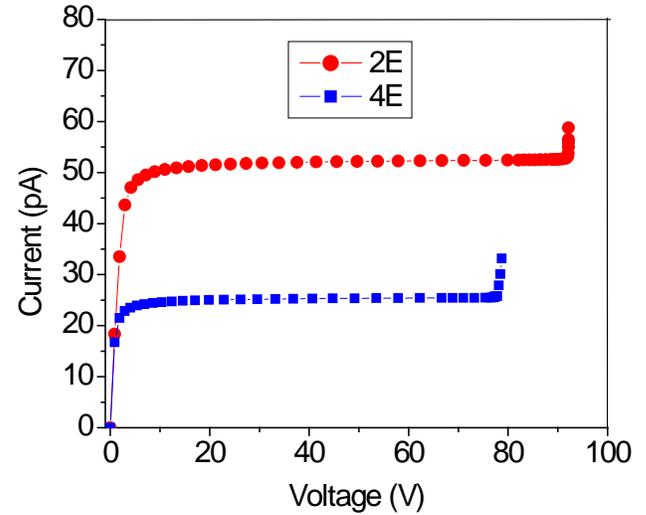
doping of the p-spray is at its maximum. As the oxide charge increases with irradiation, the effective doping concentration of the p-spray decreases and reaches its minimum value when the oxide charge saturates. This explains the decrease of maximum electric field and therefore the increase of breakdown voltage after irradiation.

.

a) 4E configuration

b) 2E configuration

Fig.6 Electric field distributions at fluence of $1x10^{16}$ n_{eq}/cm^2 throughout horizontal cross sections taken at the middle of the substrate thickness for each of 3D CMS pixel detectors. Both devices are reverse-biased at 250 V to assure full depletion.
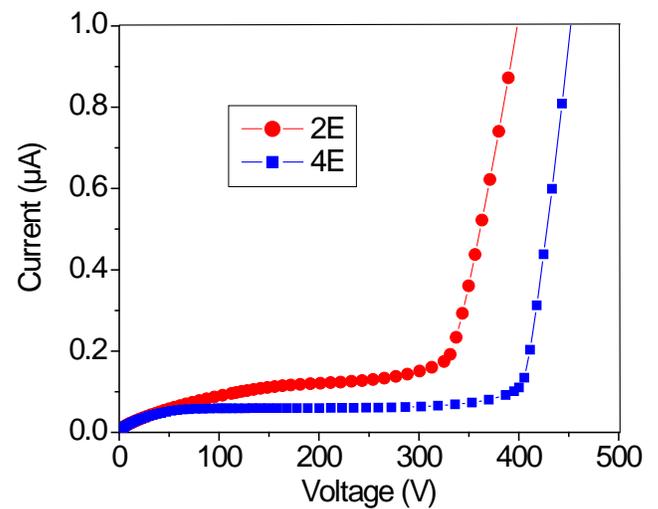
layout. A remarkable observation is that although the 2E geometry has a higher breakdown voltage before irradiation it is out-performed by the 4E geometry after irradiation.

The increase of breakdown voltage after irradiation is expected as the p-spray isolation technique is employed. This opposes p-stop isolation, in which the highest breakdown is seen before irradiation. In the case of p-spray isolation, the boron implantation dose is chosen such that it is just high enough to compensate the electron layer induced by the saturated oxide charge. Before irradiation, the p-spray concentration is drastically higher than the electron concentration on the silicon surface and the effective p-type

a)

b)

Fig.7 Leakage current behavior of the 3D CMS pixel devices at fluence of ; a) zero b) $1x10^{16} n_{eq}/cm^2$.

The charge collection efficiency has been investigated with transient simulations. Since the simulations are quite time consuming, these studies were performed only with the 4E geometry. The minimum ionizing particle (MIP) travels vertically through the entire substrate thickness and the track generates 80 electron-hole pair per micron which is the most probable energy loss for MIP travelling through silicon. The

lateral profile of the track is Gaussian with 1 µm standard deviation so more than 99.99% of the charge is generated within a radius of 2.1 µm.

The time dependence of transient current has shown that majority of the charge is collected in a fraction of 1 ns. The collected charge is obtained by integrating the transient current at the readout electrode over 5 ns. Fig.8 shows the collected charge as a function of radiation fluence when the MIP travels through the midway between the electrodes at a reverse bias of 150 V. The trapping becomes dominant after a fluence of $1x10^{15}$ n_{eq}/cm^2 and the collected charge drops to ~9.5 ke- at a fluence of $1x10^{16}$ n_{eq}/cm^2, which is 58 % of the generated

charge. When the MIP goes through the bias and readout columns, some charge can be collected before irradiation and at low fluences but the collected charge is negligibly low after a fluence of $1x10^{14}n_{eq}/cm^2$, as shown in Fig.9. Therefore, the columns become dead regions at high fluences, reducing the total sensitive area. The dead volumes comprise ~8% and ~4% of the total volume of 4E layout and 2E layout, respectively.

Fig.9 Charge collection in the 4E CMS 3D detector as a function of fluence for MIP traveling through n+ and p+ columns. The detector is reverse biased at 150 V.
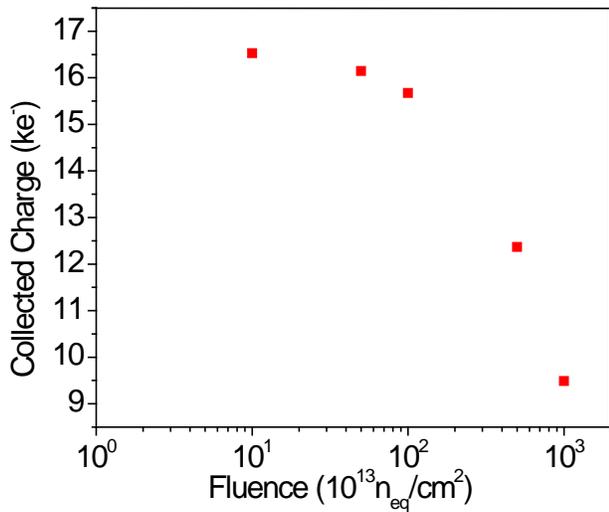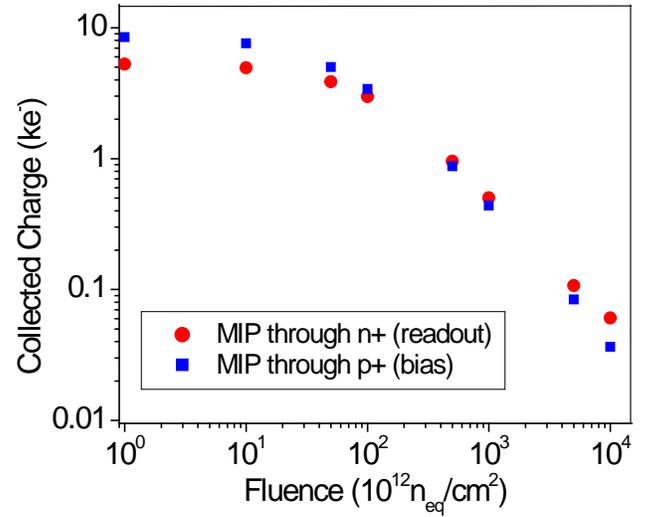

Fig.8 Charge collection in the 4E CMS 3D detector as a function of fluence for MIP passing through midway between n+ and p+ columns. The detector is reverse biased at 150 V.

The collected charge was computed for 35 different MIP positions spaced uniformly at a radiation fluence of $1x10^{16}$ n_{eq}/cm^2 and plotted as a function of x and y coordinates of the MIP (MIP direction is along the z-axis). As shown in Fig.10, the charge collection efficiency (CCE) is highest for
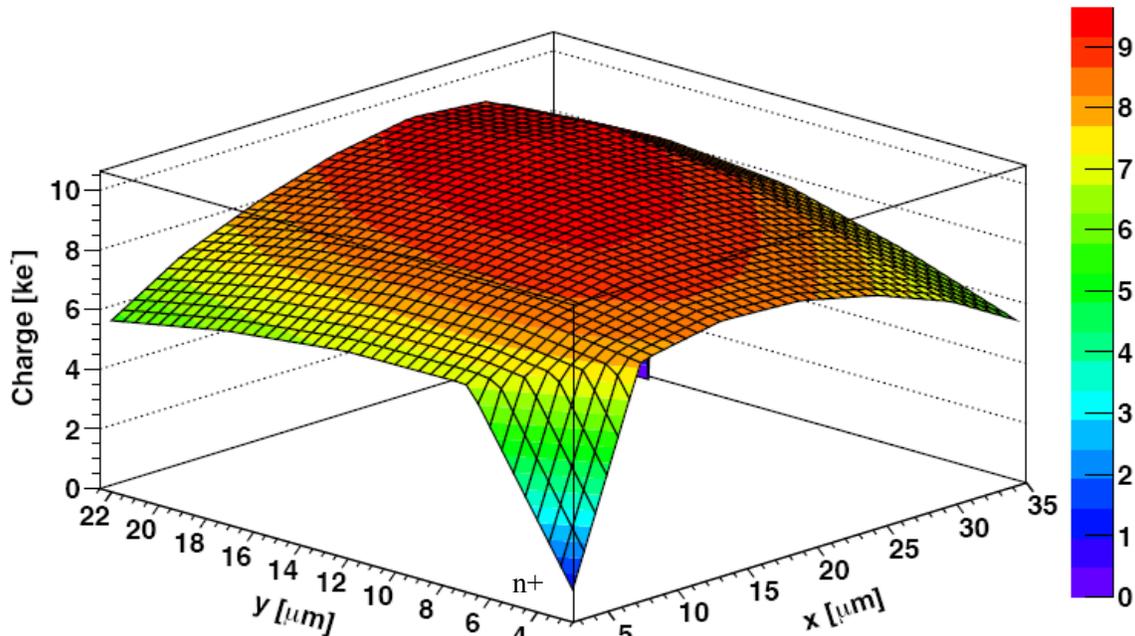

Fig.10 Variation of charge collection in the 4E CMS 3D detector with MIP position at fluence of $1x10^{16}$ n_{eq}/cm^2 . Again, the detector is biased at 150 V.

interaction points between the electrodes where it is 9.5 ke- and drops to 5.5 ke- for MIP positions near the edges. No charge is collected when MIP traverse the substrate thickness through the columns at this fluence as discussed previously. Averaging the charge collected from all MIP positions yields a CCE of 47%.

Finally, the calculation of the average CCE was repeated for different bias voltages. The variation of the CCE with bias at fluence of 1×10^{16} n_{eq}/cm^2 is shown in Fig.11. Up to the depletion voltage (80V), the collected charge increases dramatically with bias because of the obvious reason that only the charge generated in the depleted volume is collected. After the full depletion is reached, the CCE continues increasing with bias, but at a lower rate, due to the increasing electric field.
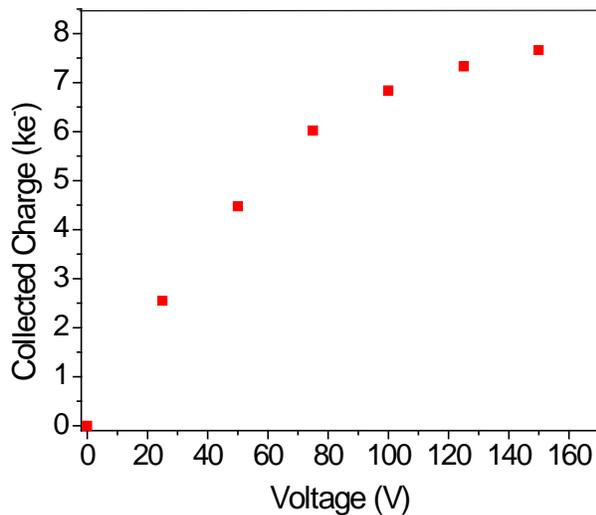

Fig.11 Average charge collection in the 4E CMS 3D detector against bias voltage at fluence of 1×10^{16} n_{eq}/cm^2

IV. FABRICATION AND FIRST TESTS OF 3D CMS PIXEL DETECTORS

A. Fabrication at SINTEF

The first run of full 3D sensor processing at SINTEF was completed in February, 2008 with 250 μm thick n-type (100) silicon wafers with resistivity of 2000 Ω.cm. These wafers include only 2E, 3E, and 4E ATLAS pixel devices along with various test structures. The isolation between n-type electrodes is provided with p-spray on front and back surfaces. The process wafer is bonded to a support wafer by direct fusion bonding after a 1 μm thermal oxidation. Holes with an aspect ratio of 14 (diameter of 18 μm) were etched using an Alcatel AMS-200 deep reactive ion etcher (DRIE) [27] with a modified Bosch process [28]. First, the n+ electrodes are etched and filled with polysilicon and then the polysilicon is doped from a gas phase source. After etching of excess polysilicon and thermal growth of a 300 nm thick oxide layer to protect the n+ electrodes, the p+ electrodes and active edge

are fabricated. At SINTEF, a polysilicon layer with thickness of ≤ 1 μm can be deposited at one time and the complete polysilicon filling is estimated to take at least 70 hours with these facilities. Therefore, after the deposition and doping of a 1 μm thick polysilicon layer at SINTEF, the rest of the electrode filling is done at Stanford Nanofabrication Facility which has the capability of depositing polysilicon layers with thickness up to 2 μm at one time. The fabrication of the electrodes is followed by the deposition and patterning of a metal layer. Finally, passivation layers of 0.5 μm oxide and 0.25μm nitride were deposited by PECVD and patterned.

The asymmetry between the oxide distribution in the front and back surfaces caused a high mechanical stress during the polysilicon filling of the columns, which resulted in a large wafer breakage in the first run. The warping of the wafers also made the alignment during the photolithographic steps extremely difficult. Large topography on the wafer surface after removal of excess polysilicon was another issue, which hindered the resist coating and photolithography. Moreover, voids and keyholes were seen in the columns after polysilicon filling mainly due to the variation in the etching profiles [29].

The second run wafers also include Medipix, 1E and 5E ATLAS, and 2E and 4E single ROC CMS devices. 200 μm and 285 μm thick p-type wafers with specific resistivity above 10,000 Ω.cm have been processed in parallel. A new deep reactive ion etcher, Alcatel AMS-200 ISPEEDER, was used for hole etching, which provides faster etching and yields trench profiles of higher quality. Another improvement in the second run is that 4 μm narrower holes were achieved. Moreover, an extra nitride layer was deposited in order to provide a better doping barrier, protect the field oxide and maintain a symmetry on the front and back surfaces. All these improvements led to significantly reduced mechanical stress, bow and breakage with 18 out of 23 wafers surviving the processing.

Fig.12 shows SEM (scanning electron microscope) images of cross section of n+ and p+ columns in a wafer from the second run after hole etching and after filling the holes with polysilicon. Much better hole profiles with fully filled n-type electrodes and only small voids in the p-type electrodes, and enhanced topography are achieved in comparison with the first run.

B. Initial Test Results

The I-V tests of the fabricated 3D CMS pixel detectors have been performed on wafer at SINTEF. Fig.13.a)-d) show the leakage current characteristics of 2E and 4E 1ROC CMS pixel sensors, respectively, from 200 μm thick (B2-1) and 285 μm thick (B5) wafers. Five chips with 2E configuration and five chips with 4E configuration from each wafer turned out to yield good I-V behaviour. All chips with 2E geometry sustain a reverse bias of 100 V without any indication of breakdown while some of the chips with 4E configuration exhibit a soft breakdown before the leakage current starts to increase dramatically. The leakage current is in the order of 1 μA/cm² before breakdown and the full depletion voltage is less than 20 V for all sensors. Furthermore, I-V measurements on different
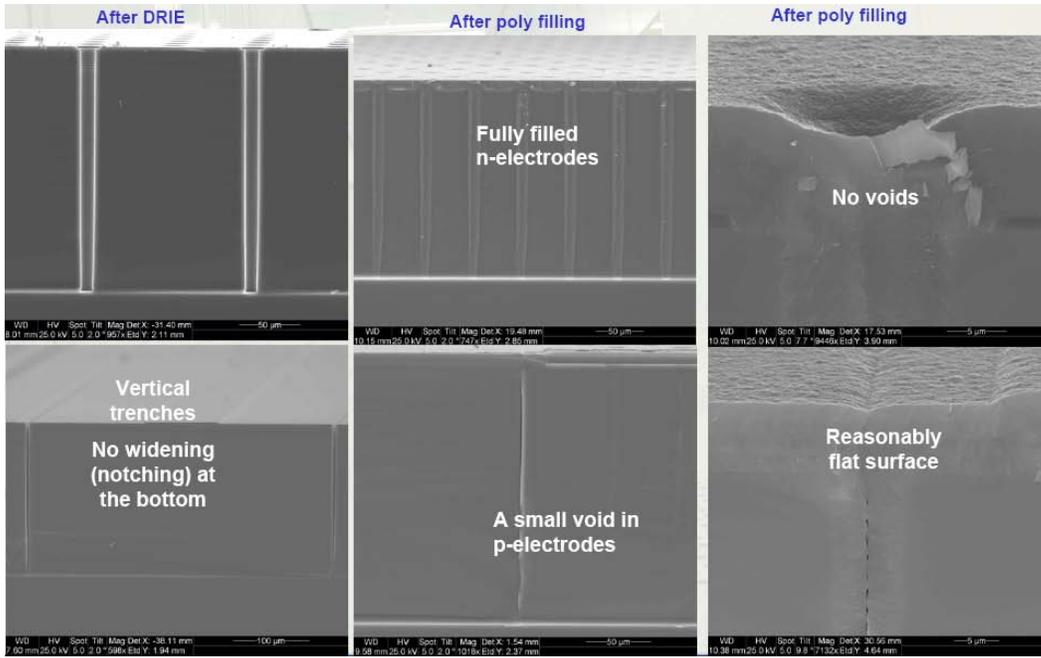
Fig.12 SEM images of the columns in second run 3D SINTEF devices before and after polysilicon filling.
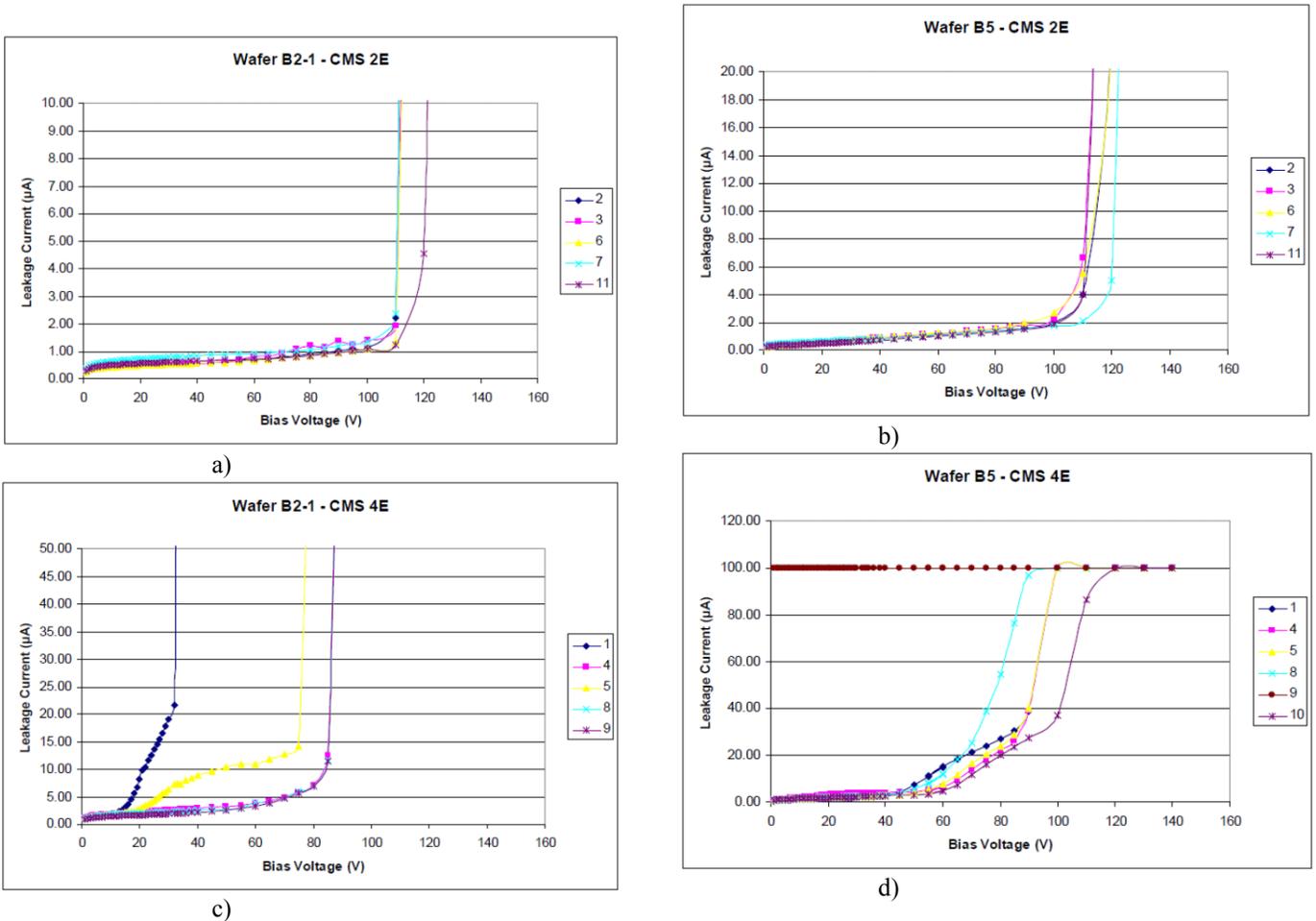

Fig.13 Leakage currents of 3D CMS pixel detectors with different configurations and substrate thickness: a) 2E configuration in 200 μm thick wafer b) 2E configuration in 285 μm thick wafer c) 4E configuration in 200 μm thick wafer d) 4E configuration in 285 μm thick wafer. The measurements were done at SINTEF at the wafer stage.

pixels have shown a typical average leakage current of 0.5 to 1 nA per pixel at full depletion.

As shown in Fig.7 a), the simulated leakage currents are ~25 pA and ~50 pA for a single cell of 2E and 4E geometries, respectively. A pixel contains 8 cells in the 4E configuration and 4 cells in the 2E configuration. Normalizing the cell currents yields a pixel current of 0.2 nA which is of the same order as the measured current. The leakage current measurements were conducted with a temporary test metallization that shorts all the n-type electrodes to obtain the total chip current in one measurement. A positively biased p-bulk MOS structure is formed with the presence of the temporary metal layer, resulting in type inversion of the silicon surface. Therefore, some of the measured current might be due to this inversion charge as well as possibly some bad pixels, which will be verified after testing the bump-bonded sensors.

The simulations showed breakdown voltages of ~80 V and ~95 V for 4E and 2E configurations, respectively. The breakdown voltage is strongly dependent on the oxide charge and these values were obtained under the assumption that oxide charge is $1x10^{11}$ cm^{-2}, which is the typical value before irradiation. Comparing the simulated breakdown voltages with the experimental values, which are ~85 V for most sensors with 4E configuration and ~110 V for most sensors with 2E configuration, it can be seen that the simulation is able to predict the breakdown voltages with a q uite reasonable accuracy.

V. CONCLUSIONS AND FUTURE WORK

The fabrication of full 3D CMS sensors at SINTEF has been completed. The I-V characteristics as measured at the wafer level are promising. Since these measurements were done with a temporary metal layer, some of the current might be due to the MOS effect so the actual leakage current will be determined by testing the bump-bonded sensors. Two processed wafers have been diced and bump-bonded with the backing wafer at IZM, Germany. The bump-bonded CMS pixel sensors will be first characterized at Purdue University with a source and then FNAL (Fermi Lab) with a test beam. The final removal of the support wafer remains a challenge. Another two processed wafers were sent back to SINTEF after only the metallization was done at IZM for the removal of the supporting wafers and dicing by DRIE at SINTEF. The expected post-irradiation electrical and charge collection performance of 3D CMS pixel detectors has been simulated using radiation damage models from literature. These simulation results will be later compared with the experimental data to check the consistency.

REFERENCES

[1] I. Parker, C.J. Kenney, J. Segal, "3D- A proposed new architecture for solid-state radiation detectors" *Nucl. Instr. and Meth. A*, vol. 395, pp. 328-343, 1997.

[2] C. Piemonte, M. Boscardin, S. Ronchin, N. Zorzi, G.-F. Dalla Betta, " Development of 3D detectors featuring columnar electrodes of the same doping type" *Nucl. Instrum. and Meth. A*, vol. 541, no. 1-2, pp. 441-448, 2005

[3] S. Ronchin, M. Boscardin, C. Piemonte, A. Pozza, N. Zorzi, G.-F. Dalla Betta, L. Bosisio and G. Pellegrini, "Fabrication of 3D detectors with columnar electrodes of the same doping type", *Nucl. Instr. and Meth. A*, vol. 573, no. 1–2, pp. 224–227, Apr. 2007.

[4] Ronchin and N. Zorzi, "First electrical characterization of 3D detectors with electrodes of the same doping type", *Nucl. Instr. and Meth. A*, vol. 570, no. 2, pp. 317–321, Jan. 2007.

[5] M. Boscardin, L. Bosisio, M. Bruzzi, G.-F. Dalla Betta, C. Piemonte, A. Pozza, S. Ronchin, C. Tosi, N. Zorzi, "Characterization of 3D-stc detectors fabricated at ITC-irst", *Nucl. Instr. and Meth. A*, vol. 572, no. 1, pp. 284–286, Mar. 2007.

[6] M. Scaringella, A. Polyakov, H.F.-W. Sadrozinski, M. Bruzzi, C. Tosi, M. Boscardin, C. Piemonte, A. Pozza, S. Ronchin, N. Zorzi and G.-F. Dalla Betta, "Charge collection measurements in single-type column 3D sensors", *Nucl. Instr. and Meth. A*, vol. 579, no. 2, pp. 638–641, Sep. 2007.

[7] M. Zavrtanik, V. Cindro, G. Kramberger, J. Langus, I. Mandi, M. Mikuz, C. Piamonte, M. Boscardin, G.-F. Dalla Betta, S. Ronchin, N.Zorzi and A. Pozza, "Position sensitive TCT evaluation of irradiated 3D STC detectors", 2007 IEEE Nuclear Science Symposium Conference Record, N24-150

[8] S. Eckert, T. Ehrich, K. Jakobs, S. Kuhn, U. Parzefall, M. Boscardin, C. Piemonte and S. Ronchin, "Signal and charge collection efficiency of a p-type STC 3D-detector irradiated to sLHC-fluences, read out with 40 MHz", *Nucl. Instr. and Meth. A*, vol. 581, no. 1–2, pp. 322–325, Oct. 2007.

[9] T. Ehrich, S. Kuhn, M. Boscardin, G.-F. Dalla Betta, S. Eckert, K. Jakobs, M. Maaßen, U. Parzefall, C. Piemonte, A. Pozza, S. Ronchinand N. Zorzi, "Laser characterisation of a 3 D single-type column p-type prototype module read out with ATLAS SCT electronics", *Nucl. Instr. and Meth. A*. vol.583, no. 1, pp. 153-156, 2007

[10] G. Pellegrini, F. Campabadal, M. Lozano, J.M. Rafi, M. Ullan, R. Bates, C. Fleta and D. Pennicard, "Double sided 3D detector technologies at CNM-IMB", *Nuclear Science Symposium Conference Record, 2006. IEEE*, vol. 2, pp. 1248–1252, Oct. 29 2006-Nov. 1 2006.

[11] D. Pennicard, G. Pellegrini, M. Lozano, R. Bates, C. Parkes, V. O'Shea and V. Wright, "Simulation results from double-sided 3-D detectors", *IEEE Trans. Nucl. Sci.*, vol. 54, no. 4, pp.1435-1443, Aug. 2007.

[12] G. Pellegrini, M. Lozano, M. Ullán, R. Bates, C. Fleta and D. Pennicard; "First double-sided 3-D detectors fabricated at CNM-IMB", *Nucl. Instrum. and Meth. A*, vol. 592, pp. 38-43, 2008

[13] G.-F. Dalla Betta, M. Boscardin, L. B osisio, G. Darbo, P.Gabos, C. Gemme, M. Koehler, A. La Rosa, U. Parzefall, H. Pernegger, C. Piemonte, M. Povoli, I. Rachevskaia, S. Ronchin, L. Wiik, A. Zoboli, N. Zorzi, "Characterization of 3D-DDTC detectors on p-type substrates", arXiv:0911.4864

[14] A. La Rosa et al. "Preliminary results of 3D-DDTC pixel detectors for the ATLAS upgrade", arXiv:0910.3788

[15] R. Bates, "Charge collection studies of irradiated 3D detectors", 15th RD50 Workshop, CERN, 16–18 November 2009, available online at http://rd50.web.cern.ch/rd50/

[16] C. Kenney, S. Parker, J. Segal and C. Storment, "Silicon detectors with 3D electrode arrays: fabrication and initial test results", *IEEE Trans. Nucl. Sci.*, vol. 46, no. 4, pp. 1224-1236, Aug. 1999

[17] C.J. Kenney, S.I. Parker and E. Walckiers, "Results from 3D sensors with wall electrodes:near-cell-edge sensitivity measurements as a preview of active-edge sensors", *IEEE Trans. Nucl. Sci.*, vol. 48, no. 6, pp. 2405-2410, December 2001

[18] C. Da Via, J. Hasi, C. Kenney, A. Kok and S. Parker, "3D silicon detectors — Status and applications", *Nucl. Instrum. Meth. A*, vol. 549, no. 1-3, pp. 122-125, 2005

[19] A. Kok, G. Anelli, C. DaVia, J. Hasi, P. Jarron, C. Kenny, J. Morse, S. Parker, J. Segal, S. Watts and E. Westbrook "3D detectors — State of the art", *Nucl. Instrum Meth. A,* vol. 560**,** no.1, pp. 127-130, 2006

[20] C.J. Kenney, J.D. Segal, E. WestBrook, S. Parker, J. Hasi, C. DaVia, S. Watts and J. Morse, "Active-edge planar radiation sensors", *Nucl. Instrum. Meth. A,* vol. 565**,** no. 1, pp. 272-277, 2006

[21] M. Petasecca, F. Moscatelli, D. Passeri, G.U. Pignatel, "Numerical simulation of radiation damage effects in p-type and n-type FZ silicon detectors", *IEEE Trans. Nucl. Sci.,* vol. 53, no.5, pp. 2971-2976, 2006

[22] D. Pennicard, C. Fleta, R. Bates, V. O'Shea, C. Parkes, G. Pellegrini, N. Tartoni, "Simulations of radiation-damaged 3D detectors for the Super-LHC", *Nucl. Instrum. Meth. A*, vol. 592, pp. 16-25, 2008

[23] G. Kramberger, V. Cindro, I. Mandic and M. Mikuz, "Impact of annealing of trapping times on charge collection in irradiated silicon detectors" *Nucl. Instr. and Meth. A* vol. 579, no.2, pp. 762-765, 2007

[24] Synopsys Inc., Synopsys TCAD Manuals, <http://www.synopsys.com/products/tcad/tcad.html>, 2007

[25] V.A. Wright, W.D. Davidson, J.J. Melone, V. O'Shea, K.M. Smith, L. Donohue, L. Lea, K. Robb, S. Nenonen and H. Sipila, **"**Three-dimensional Medipix-a new generation of X-ray detectors", *IEEE Trans. Nucl. Sci.* NS-52 (5), pp. 1873-1876, 2005

[26] Y. Okuto and C. R. Crowell, "Threshold energy effect on avalanche breakdown voltage in semiconductor junctions" *Solid-State Electronics*, vol. 18, no. 2, pp. 161-168, 1975

[27] Alcatel AMS-200, http://www.alcatelmicromachining.com.

[28] F. Laermer and A. Schilp, "Method of anisotropically etching silicon", US-Patent No 5501893, Robert Bosch GmbH (1996).

[29] T.E. Hansen, A. Kok, T.A. Hansen, N. Lietaer, M. Mielnik, P. Storas, C. DaVia, J. Hasi, C. Kenney and S. Parker, "First fabrication of full 3D-detectors at SINTEF", *JINST,* 4:P03010,2009